



Defect-engineered WO_{3-x}@MoS₂ hollow tube exhibiting enhanced Fenton-like and photocatalytic activities via electric field rearrangement and band alignment

Yi Hu^{a,1}, Mingxing Nie^{a,c,1}, Peidong Hong^{a,*}, Junyong He^a, Yulian Li^a, Kaisheng Zhang^a, Dandan Yang^{a,c}, Lisha Jiang^{b,*}, Jinhui Liu^a, Lingtao Kong^{a,*}

^a Environmental Materials and Pollution Control Laboratory, Institute of Solid State Physics, Chinese Academy of Sciences, Hefei 230031, China

^b School of Environmental and Materials Engineering, Yantai University, Yantai 264005, China

^c University of Science and Technology of China, Hefei 230026, China

ARTICLE INFO

Keywords:

WO_{3-x}@MoS₂ hollow tube
Electric field rearrangement
Band alignment
Fenton-like
Environmental photocatalyst

ABSTRACT

Here we report a defect-engineered WO_{3-x}@MoS₂ hollow tube that exhibits not only enhanced Fenton-like activity but also improved photoactivity in a wide range of pH as a versatile platform for water purification. Its successful performance was achieved by tuning oxygen defect and band position and investigated using tetracycline degradation and *E. coli* inactivation experiments as concept demonstration. The activity of WO_{3-x}@MoS₂ can reach one to two orders of magnitude higher than that of other materials used in this work and the ecotoxicity of intermediates was largely reduced. It exhibits an intrinsic radical character for H₂O₂ decomposition under dark condition and an efficient photon utilization under visible light irradiation, which is clearly different from the conventional photocatalysts and Fenton reagents. The present strategy of combining the dark Fenton-like and photocatalytic activities extends the applications of the conventional photocatalysts and should be an efficient way of energy utilization.

1. Introduction

How to achieve the efficient removal of contaminants and the reasonable utilization of energy are currently attracting increasing interest because of the environmental and energy crisis. Of the various approaches of wastewater treatment and sustainable chemistry engineering reported to date, photocatalysis is considered as an eco-friendly candidate for realizing environmental purification and counteracting energy shortage via solar energy [1,2]. WO₃ as a n-type semiconductor photocatalyst has been extensively adopted to water purification [3], volatile organic compounds (VOC) removal [4], H₂ evolution and water oxidation [3,5]. Despite these merits, photodegradation using WO₃ still faces practical challenges. The instantaneous recombination of photo-generated hole-electron pairs limits its direct application. How to enhance the carrier utilization has thus become the key point for pushing forward the evolution of WO₃ photocatalysts. One approach is to decorate WO₃ with another semiconductor with appropriate band alignment. Typical examples are BiVO₄-WO₃ heterojunction [6] and

WO₃-g-C₃N₄ 2D/2D ultrathin step-like composite [7], in which the formed interfacial contact can promote charge transfer and separation, and lead to an enhanced photocatalytic activity. Another issue that limits the environmental application of WO₃ semiconductor is the requisite of light irradiation for achieving redox reaction. Once the light source is cut off, charge excitation and transfer are suspended and WO₃ immediately becomes catalytically inert. Recent researches have explored the “memory effect”, which enables the photocatalysts to remain the activity in the dark for a period. Cai et al. reported that “dark deposition” of Ag nanoparticles on TiO₂ can act as a round-the-clock catalyst for the degradation of multicomponent pollutants [8]. Such a merit can be attributed to the dark deposition inhibiting the formation of Ag₂O and thus improve the electron storage capacity. Chiou et al. found that the single crystalline Se nanorods remain catalytic activity under post-irradiation dark condition because of the sustained •OH radicals generation on the solid-liquid interface [9]. Engineered WO₃ photocatalyst that exhibits lasting and robust catalytic activity should be a promising candidate for wide distributed environmental applications.

* Corresponding authors.

E-mail addresses: hpd221@issp.ac.cn (P. Hong), jianglisha0112@ytu.edu.cn (L. Jiang), ltkong@iim.ac.cn (L. Kong).

¹ These authors contributed equally to this work.

Fenton system is an efficient advanced oxidation process (AOP) exhibiting indiscriminate oxidation capacity towards industrial multi-component pollutants. However, the traditional homogeneous Fenton process ($\text{Fe(II)/H}_2\text{O}_2$) has some shortcomings: (1) narrow optimal pH range (2–4); (2) generation of iron-containing sludge; (3) catalyst loss in the effluent and (4) acid or metal ions induced secondary pollution. Heterogeneous Fenton-like oxidation has been developed to overcome the above problems [10,11]. Designing WO_3 photocatalyst exhibiting Fenton-like activity should be an interesting strategy to enhance the photon utilization and H_2O_2 activation [12].

In this work, we report a defect-engineered WO_{3-x} @ MoS_2 hollow tube that exhibits enhanced Fenton-like and photocatalytic activities via electric field rearrangement and band alignment and demonstrate its successful performance as a versatile platform for water purification in a wide range of pH. MoS_2 as a p-type semiconductor with large surface area and abundant active sites was employed to construct a p-n heterojunction on WO_{3-x} . It exhibits an intrinsic radical character and a high carrier separation for H_2O_2 activation and O_2 reduction by tuning the oxygen defect and band position. As a proof of concept, the activity of WO_{3-x} @ MoS_2 for tetracycline (TC) degradation can reach one to two orders of magnitude higher than that of other materials used in this work. LC-MS analysis and theoretical calculations confirm that the intermediates were turned to be “non-toxic” and their ecotoxicity decreased during the oxidation process. The present strategy of combining the dark Fenton-like and photocatalytic activities extends the application of the conventional photocatalysts and should be an efficient way of energy utilization.

2. Experimental section

Chemical reagents used in this study are listed in Table S1. They are of all analytical grade and used without further purification. Milli-Q water was used in all experiments unless otherwise stated.

2.1. Materials preparation

Preparation of WO_{3-x} rods: The WO_{3-x} rods were prepared by modifying the literature method [13,14]. In detail, a mixture of $\text{Na}_2\text{WO}_4 \cdot 2\text{H}_2\text{O}$ (4.5 mmol), NaCl (0.6 g) and $\text{C}_2\text{H}_5\text{NO}_2$ (0.0113 g, 0.15 mmol) were added to 30 mL aqueous solution, and the pH value of the solution was adjusted to 2 by dropping 3 mol/L HCl solution. Then the obtained colorless and transparent solution was stirred for 30 min and transferred into a 50 mL PFA-lined autoclave, maintaining heated at 180 °C for 24 h and cooled down to room temperature (RT). The light blue precipitates were separated from the mother liquor by centrifugation and subsequently washed with deionized (DI) water and ethanol several times to remove the soluble impurities. Finally, the obtained powder was freeze-dried at – 40 °C overnight to yield the WO_{3-x} sample.

Preparation of WO_{3-x} @ MoS_2 hollow tube heterojunction: 0.15 g of WO_{3-x} was added into 60 mL of glucose solution (0.75 M), stirred for 30 min, and sonicated for 30 min to form a well dispersed suspension. Then 0.6 g of sodium molybdate ($\text{Na}_2\text{MoO}_4 \cdot 2\text{H}_2\text{O}$) and 1.2 g of thiourea ($\text{CH}_4\text{N}_2\text{S}$) were added and stirred for 60 min. After that, the mixed solution was transferred into a 100 mL PFA-lined autoclave, heated at 200 °C for 24 h and cooled down to room temperature. Finally, the obtained powder was washed with DI water and ethanol several times and freeze-dried at – 40 °C overnight to yield the WO_{3-x} @ MoS_2 sample.

2.2. Materials characterization

Scanning electron microscope (SEM), transmission electron microscope (TEM) and X-ray diffraction (XRD) were used to characterize the morphology and structure of materials. The specific surface area and the average pore distribution of samples was measured by Brunauer-

Emmett-Teller (BET) method. X-ray photoelectron spectroscopy (XPS) and Fourier transform infrared spectroscopy (FT-IR) were performed to investigate the chemical states of the elements and the functional groups on the catalyst surface. Electron paramagnetic resonance (EPR) spectra were obtained using a JEOL JES-FA 200 EPR spectrometer. The UV-vis diffuse reflectance spectra (DRS) and the steady-state photoluminescence (PL) emission spectra were measured using a UV3600-MPC3100 spectrophotometer and a FluoroMax-4 fluorescence spectrometer, respectively.

2.3. Fenton-like and photocatalytic activity tests

WO_{3-x} @ MoS_2 / H_2O_2 Fenton-like system was evaluated by monitoring the degradation of TC under dark condition. As control samples to be compared with WO_{3-x} @ MoS_2 , several heterogeneous Fenton-like catalysts (i.e., cubic Fe_2O_3 , spherical Fe_3O_4 , oxygen deficient WO_{3-x} , hierarchical MoS_2) were synthesized in the laboratory or purchased (commercial Fe_2O_3 , Fe_3O_4 , WO_3 from Sinopharm Chemical Reagent Co., Ltd). Their preparation methods and morphology characterizations are shown in Text S1 and Fig. S1, respectively. In each test, 30 mg of catalyst sample was dispersed in 100 mL of 100 μM TC aqueous solution containing 15 mM H_2O_2 . The pH value was adjusted using HCl and NaOH solution and measured by a pH meter. The water samples were collected at given reaction time and filtered with membrane filters (0.22 μm) to remove catalyst particles prior to analysis. All the experiments were performed in triplicate unless stated otherwise. pH- and H_2O_2 -dependence experiments were conducted to investigate their influence on performing WO_{3-x} @ MoS_2 / H_2O_2 Fenton-like oxidation. The adsorption equilibrium (20 min) was established prior to degradation experiments. Detailed conditions and kinetic models are shown in Table S2 and Text S2.

Photo-Fenton-like and photocatalytic activity tests were as follows: the suspension was magnetically stirred for 20 min in the dark to establish the ad/desorption equilibrium of TC on the surface of catalysts. After that, visible-light irradiation was achieved by using a 300 W Xenon lamp with a 420 nm cut-off filter. Water samples were collected at given reaction time and filtered with membrane filters (0.22 μm) to remove the catalyst particles prior to analysis.

The bacterial inactivation experiments were conducted with *E. coli* following the previous method [15,16]. *E. coli* culture was diluted to obtain ca. $\sim 6 \times 10^5$ colony forming units per milliliter (CFU/mL) as bacterial stock solution. The test water samples were withdrawn intermittently and diluted with sterilized water by 10, 100 and 1000 times. Then 0.1 mL diluted samples were evenly spread on the nutrient agar plates and incubated at 42 °C for 18 h to form obvious bacterial colonies.

2.4. Analytical methods

The concentration of substrates was measured by using a UV-visible spectrophotometer and a high performance liquid chromatograph (HPLC, Agilent 1260 Infinity). A total organic carbon (TOC) analyzer was employed to investigate the TC mineralization (Text S2). The intermediates of TC degradation were detected by using a liquid chromatography-mass spectrometer (LC-MS).

2.5. (Photo)electrochemical measurements

The electrochemical impedance spectroscopy (EIS) profiles were obtained using a Ag/AgCl electrode and a Pt wire as the reference and counter electrodes, respectively [15,17,18]. Visible light irradiation was achieved by a 300 W Xenon lamp with a 420 nm cutoff filter. 0.1 M NaClO_4 solution was used as an electrolyte. The linear sweep voltammetry (LSV) measurements were performed in N_2 -saturated 0.1 M KOH solution containing 15 mM H_2O_2 under the dark condition [19,20].

2.6. Computational details

The theoretical calculation of structural optimization was employed to investigate the details of intermediates. By calculating the EE2 minimization energy, the possible intermediates generated from the dehydration and dehydrogenation processes were proposed. The biological toxicity of TC and its intermediates was evaluated using the toxicity evaluation software tool (T.E.S.T, version 4.2.1, see Text S3) [21]. The charge density difference and work functions were calculated by VASP (Vienna Ab-initio Simulation Package) [17,22,23].

3. Results and discussion

3.1. Materials characterization

SEM and TEM images (Fig. 1a1–a4) show that the diameter of WO_{3-x} is lower than 120 nm and the length extends to 5 μm . The fringes with the interplanar spacing of cal. 3.1 Å can be assigned to the (200) planes of WO_3 . Fig. 1b1–b4 shows that the MoS_2 nanosheets were uniformly coated on WO_{3-x} tubes and the hollow structure of $\text{WO}_{3-x}@\text{MoS}_2$ were clearly visible in the yellow frame. The morphology evolution from nanorods to hollow tube can be explained by the alkali etching mechanism, which demonstrates a classic hydrothermal reaction that the NH_3 produced by thiourea at high temperature will preferentially etch the interior of WO_3 rod and make it hollow and porous [24–27]. The produced NH_3 can etch WO_{3-x} nanorods and the CO_2 generated from the pyrolysis of thiourea and glucose can increase the pressure and form gaseous cavities under hydrothermal growth conditions, which can affect the local pH and hinder the heterogeneous nucleation. This limitation is more inclined to occur inside the WO_{3-x} rod because of the local high pressure and the narrow reaction surface. The different chemical environment inside and outside of WO_{3-x} nanorods makes MoS_2 prefer to grow on the surface of WO_{3-x} and thus the internal hollow structure is remained. The ordered lattice fringes with a spacing

of 3.1 Å, 3.8 Å and 6 Å can be assigned to the crystalline of (200) WO_3 , (001) WO_3 and (002) MoS_2 respectively. EDS elemental mapping analysis shows the uniform distributions of W, O, Mo and S elements over $\text{WO}_{3-x}@\text{MoS}_2$ (Fig. 1c1–c6).

In XRD profile (Fig. S2), the WO_{3-x} is well indexed to hexagonal phase WO_3 (JCPDS No.33–1387) and the $\text{WO}_{3-x}@\text{MoS}_2$ pattern matches well with the peaks of WO_{3-x} and MoS_2 (JCPDS No. 87–2416) [28,29]. Fig. S3 shows the FTIR spectra of as-obtained WO_{3-x} and $\text{WO}_{3-x}@\text{MoS}_2$ samples. The band positions at 3445 and 1628 cm^{-1} can be attributed to the stretching vibration of OH and the blending vibration of H-O-H, respectively. The band at 1399 cm^{-1} is related to the vibration of O-H in W-OH. The band at 835 cm^{-1} is assigned to the absorption of W-O bind, and the decrease of W-O signal in $\text{WO}_{3-x}@\text{MoS}_2$ indicates that the MoS_2 nanosheets were successfully coated on the surface of WO_{3-x} [30]. Nitrogen adsorption-desorption isotherm and the corresponding pore-size distribution curves (Fig. S4) show that the surface area of $\text{WO}_{3-x}@\text{MoS}_2$ and MoS_2 are 60 and 45 m^2/g respectively, while the surface area of WO_{3-x} is only 8.4 m^2/g . The increased surface area for $\text{WO}_{3-x}@\text{MoS}_2$ should be attributed to the formation of the hollow structure. The XPS profile shown in Fig. S5 confirms the existence of W, O, Mo and S elements on the surface of $\text{WO}_{3-x}@\text{MoS}_2$. The inset in Fig. 2a shows that the W 4f XPS profile of $\text{WO}_{3-x}@\text{MoS}_2$ slightly shifts to the lower binding energy, which indicates the variety of chemical environments of W atoms [31,32]. The peaks at 36.77, 38.97, 35.66, 37.86 eV can be attributed to $\text{W}^{6+} 4f_{7/2}$, $\text{W}^{6+} 4f_{5/2}$, $\text{W}^{5+} 4f_{7/2}$ and $\text{W}^{5+} 4f_{5/2}$, respectively [33]. The O 1s XPS profile of $\text{WO}_{3-x}@\text{MoS}_2$ hollow tube is presented in Fig. 2b. Four peaks at 530.93, 531.8, 532.26 and 533.14 eV are the characteristic signals of the lattice oxygen, surface adsorbed oxygen, oxygen vacancy and hydroxyl oxygen, respectively [33,34]. The High resolution W 4f and O 1s XPS profiles of WO_{3-x} rods were shown in Fig. S6. It is generally accepted that the formation of oxygen vacancies leads to the generation of W^{5+} centers and unpaired electrons, which increases the donor levels in the electronic structure of transition metal oxide and facilitates the charge

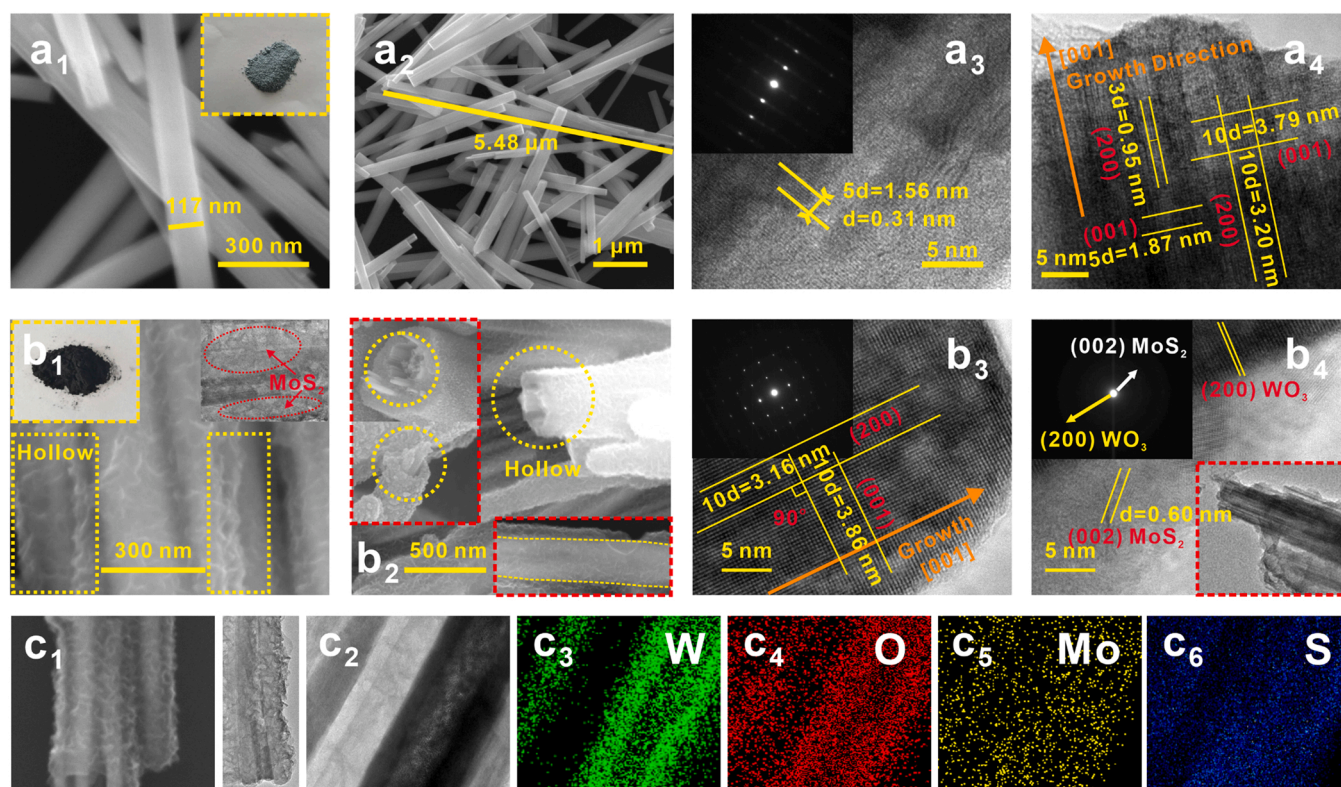


Fig. 1. SEM and HRTEM images of (a) WO_{3-x} and (b) $\text{WO}_{3-x}@\text{MoS}_2$. (c) EDS elemental mapping profiles of W (green), O (red), Mo (yellow) and S (blue) elements over $\text{WO}_{3-x}@\text{MoS}_2$.

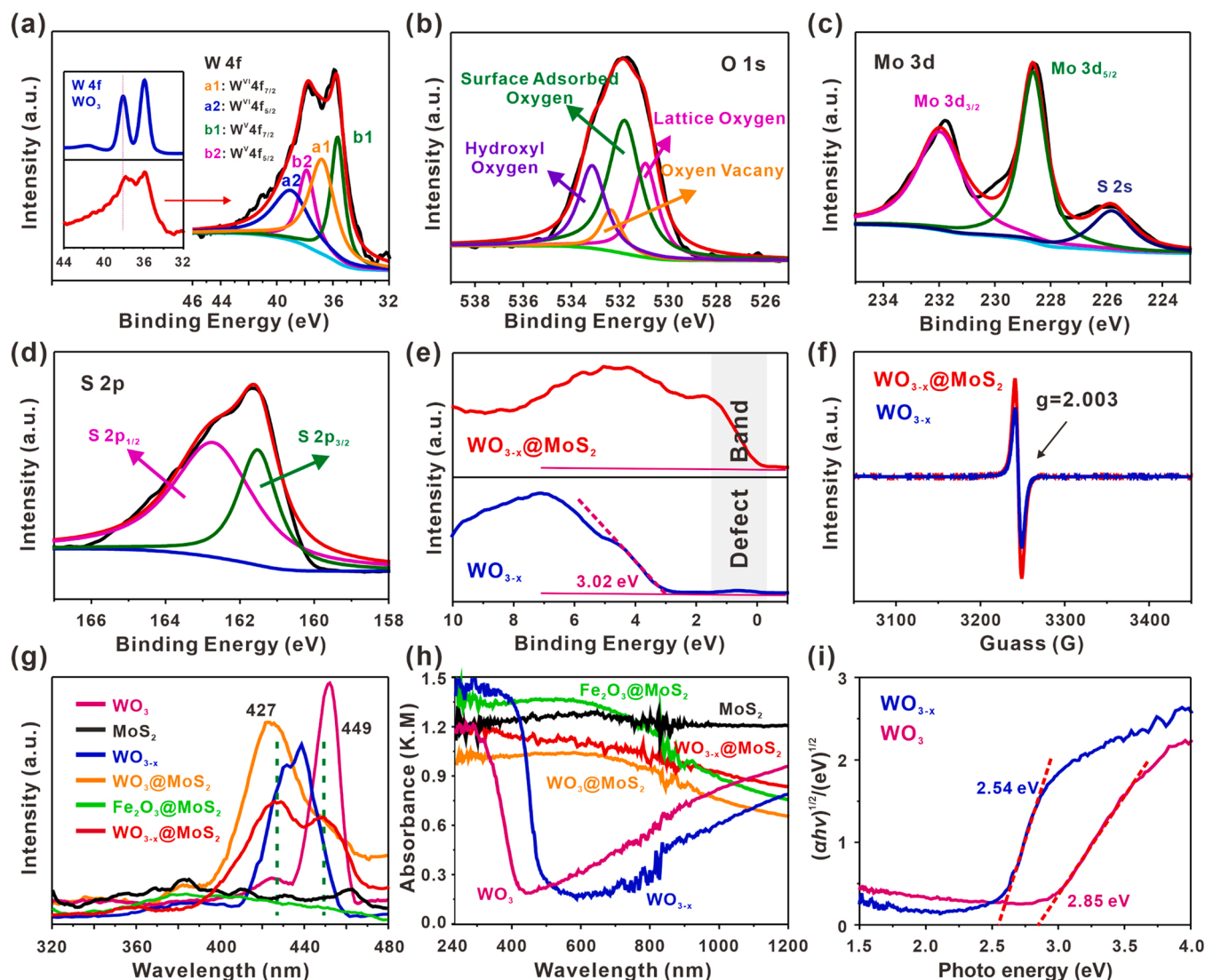


Fig. 2. High resolution XPS profiles of (a) W 4f, (b) O 1s, (c) Mo 3d, (d) S 2p, (e) XPS valence band spectra and (f) EPR spectra of WO_{3-x} and $\text{WO}_{3-x}@\text{MoS}_2$ samples obtained at room temperature. (g) PL spectra and (h) UV-vis DRS of MoS_2 , bare WO_3 , WO_{3-x} , $\text{Fe}_2\text{O}_3@\text{MoS}_2$, $\text{WO}_3@\text{MoS}_2$ and $\text{WO}_{3-x}@\text{MoS}_2$ samples. (i) the plots of $(\alpha h\nu)^{1/2}$ vs photon energy ($h\nu$) for the band gap energy of bare WO_3 and WO_{3-x} .

separation on the semiconductor-electrolyte interface. Fig. 2c shows the Mo 3d XPS profile and it can be resolved into three characteristic peaks. The two peaks at 228.63 and 231.96 eV are assigned to Mo 3d_{5/2} and Mo 3d_{3/2} respectively, and the other peak at 225.80 eV can be attributed to S 2s [28]. The S 2p high-resolution XPS profile can be divided into two peaks at 161.58 and 162.75 eV, corresponding to S 2p_{3/2} and S 2p_{1/2}, respectively (Fig. 2d). On the other hand, a sub-level that emerges near Fermi energy level (E_F) of WO_{3-x} and $\text{WO}_{3-x}@\text{MoS}_2$ (Fig. 2e) can be attributed to the defect band (DB) level that induced by the localized electrons in the d-orbitals of low valence W_W species [31,35]. The EPR spectra obtained at room temperature (Fig. 2f) exhibit one single Lorentzian line with the g value of 2.0032 for WO_{3-x} and $\text{WO}_{3-x}@\text{MoS}_2$, which can be ascribed to the unpaired electron derived from the oxygen vacancies [35–38]. Fig. 2g shows the PL emission spectra of $\text{WO}_{3-x}@\text{MoS}_2$ and the control samples. The PL intensity of $\text{WO}_{3-x}@\text{MoS}_2$ hollow tube is smaller than that of WO_{3-x} and $\text{WO}_3@\text{MoS}_2$, resulting a longer lifetime of carriers and the enhanced photoactivity [33]. Two typical peaks at 427 and 449 nm can be attributed to the band edge emission and O_V defect-state emission [39,40]. Fig. 2h shows the UV-visible DRS of the as-prepared samples. WO_{3-x} exhibits a wider range of visible light response than WO_3 while the $\text{WO}_{3-x}@\text{MoS}_2$

hollow tube displays the stronger absorption in the spectrum than WO_{3-x} and $\text{WO}_3@\text{MoS}_2$. By plotting $(\alpha h\nu)^{1/2}$ vs. $h\nu$ from the adsorption spectra and then extrapolating the linear region to the abscissa, the band gap value was estimated at 2.54 eV for WO_{3-x} which is smaller than that of bare WO_3 (2.85 eV) (Fig. 2i).

3.2. Fenton-like and photocatalytic activities of $\text{WO}_{3-x}@\text{MoS}_2$

The dark Fenton-like activity of $\text{WO}_{3-x}@\text{MoS}_2$ was compared with other samples (iron oxide or tungsten oxide-based catalysts) (Fig. 3a). The pH value was not adjusted at all in the activity tests. The bare samples of Fe_2O_3 , Fe_3O_4 , WO_3 and WO_{3-x} exhibited insignificant activity while the hierarchical MoS_2 displayed the unexpected performance for TC removal. Control adsorption experiment and kinetic model (Fig. S7) confirms that such a quick TC removal was attributed to the adsorption behavior of MoS_2 . $\text{WO}_{3-x}@\text{MoS}_2$ exhibited the highest activity in TC degradation among these catalysts. On the other hand, iron oxide and tungsten oxide-based samples were used as control groups in pH- and H_2O_2 -dependence experiments (Figs. S8 and S9). Fig. 3b shows that the $\text{WO}_{3-x}@\text{MoS}_2$ exhibits the highest activity in the set pH range and the best performance can be achieved around pH 3–4. Furthermore,

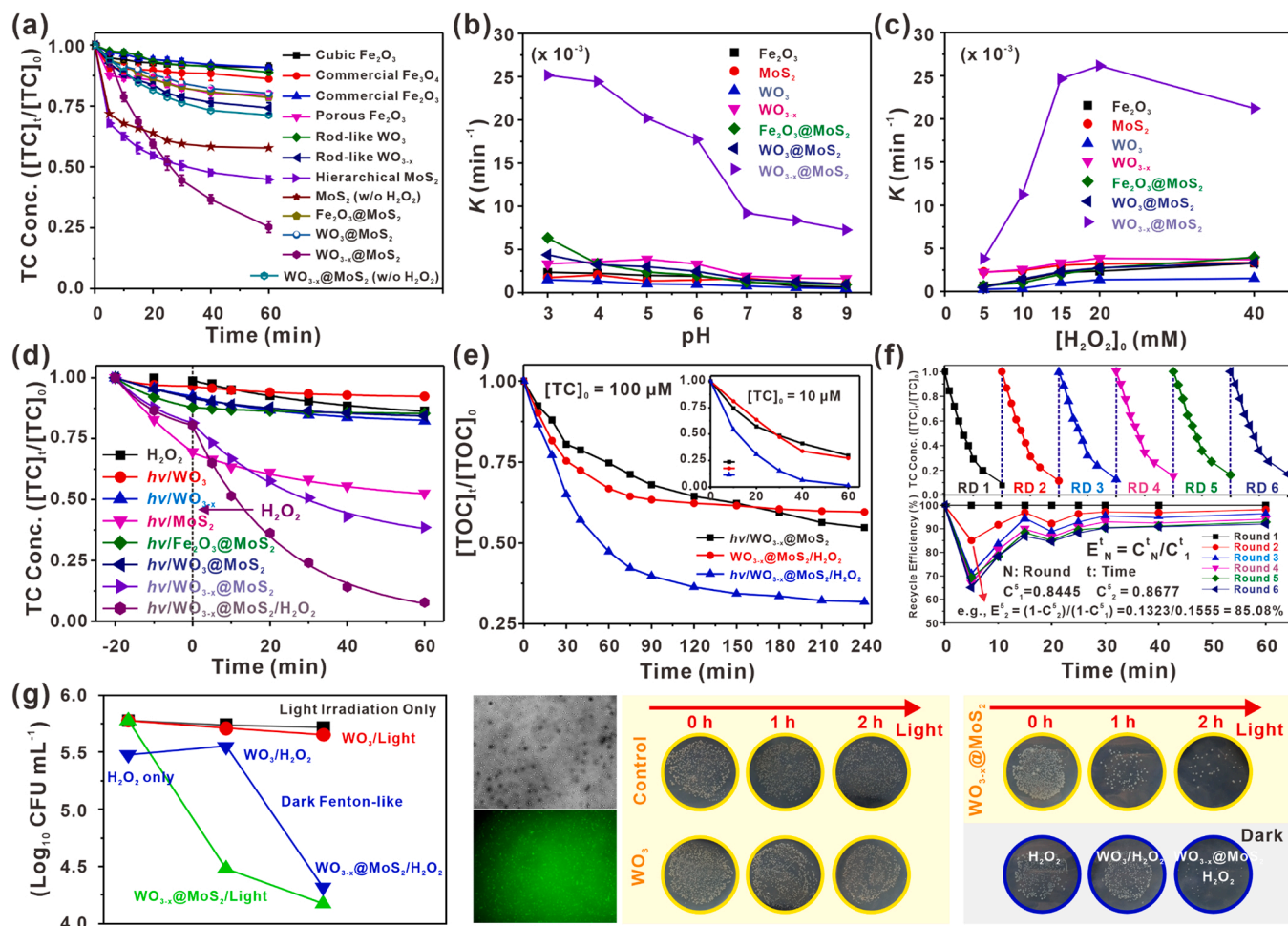


Fig. 3. (a) Time profiles of TC degradation under different dark Fenton-like systems. Experimental conditions: [catalyst] = 0.3 g/L, [H₂O₂]₀ = 15 mM, RT. The initial pH of the catalyst suspension was not adjusted. Cubic Fe₂O₃/H₂O₂, pH = 5.62; commercial Fe₂O₃/H₂O₂, pH = 6.00; porous Fe₂O₃/H₂O₂, pH = 5.79; commercial Fe₂O₃/H₂O₂, pH = 5.12; bare WO₃/H₂O₂, pH = 6.10; WO_{3-x}/H₂O₂, pH = 6.61; hierarchical MoS₂/H₂O₂, pH = 2.91; Fe₂O₃@MoS₂/H₂O₂, pH = 5.21; WO₃@MoS₂/H₂O₂, pH = 4.35; WO_{3-x}@MoS₂/H₂O₂, pH = 5.63. (b) The degradation rate constant (k) as a function of pH. (c) k as a function of initial H₂O₂ concentration. (d) Time profiles of TC degradation under visible light irradiation. Experimental conditions: [catalyst] = 0.3 g/L, [H₂O₂]₀ = 15 mM, [TC]₀ = 100 μM, pH = 6 ± 0.2, light irradiation was achieved at 0 min by a 300 W Xenon lamp with a 420 nm cut-off filter. (e) Time profiles of TOC removal in different catalytic processes, [TOC]₀ = 26.4 mg/L. (f) Reusability of WO_{3-x}@MoS₂ hollow tube for the removal of TC during six successive runs under visible light irradiation. (g) Inactivation of *E. coli* in the photocatalytic and dark Fenton-like ([H₂O₂]₀ = 1 mM) systems.

the Fenton activity of WO_{3-x}@MoS₂ rapidly increased with [H₂O₂]₀ and reaches the saturation around 20 mM, whereas that of other catalysts was little enhanced even up to [H₂O₂]₀ = 40 mM (Fig. 3c). For the case of 15 mM H₂O₂ and pH 6, the ~6% performance difference for WO_{3-x}@MoS₂ is from the experimental error since the [H₂O₂]₀- and pH-dependence experiments for WO_{3-x}@MoS₂ were carried out independently (Table S2).

The photoactivity of WO_{3-x}@MoS₂ was tested and compared with other catalysts. The control case of H₂O₂ alone, bare WO₃ and Fe₂O₃@MoS₂ exhibited insignificant photoactivity whereas WO_{3-x}@MoS₂ was far more efficient under visible light irradiation and can be further enhanced with the presence of H₂O₂ (Figs. 3d and S10). It should be noted that the hierarchical MoS₂ alone exhibited significant adsorption performance for TC removal during the first 20 min while its catalytic activity was limited. Fig. 3e compares the efficiencies of TC mineralization in dark Fenton-like, photo-Fenton-like and photocatalytic processes. Only 30% of TOC was removed in WO_{3-x}@MoS₂ photocatalytic and dark Fenton-like processes whereas the photo-Fenton-like system was more efficient. On the other hand, WO_{3-x}@MoS₂ photo-Fenton-like system exhibited the excellent performance in the mineralization of low-concentration pollutants within a short time as 10 μM of TC can be completely mineralized within 60 min. The catalytic activity of WO_{3-x}@

@MoS₂ was further investigated during six successive runs under visible light irradiation (Fig. 3f). The degradation rates of TC on WO_{3-x}@MoS₂ were largely maintained over the course of repetitive cycles and the slight decrease can be attributed to the loss of catalysts in the collection.

Based on the observation of the enhanced (photo)-Fenton-like and photocatalytic activities, WO_{3-x}@MoS₂ was tested for the inactivation of waterborne bacteria *E. coli*. Fig. 3g shows that the visible light irradiation alone induced no microbial inactivation and that bare WO₃ exhibited a minor photocatalytic inactivation activity, and that WO_{3-x}@MoS₂ hollow tube shows the highly enhanced photocatalytic activity of *E. coli* inactivation. Compared with the control case of H₂O₂ alone under dark condition, WO₃/H₂O₂ didn't exhibited any improved inactivation activity whereas WO_{3-x}@MoS₂/H₂O₂ was far more efficient in deactivating *E. coli*.

3.3. Intrinsic radical character and charge carrier dynamics

Scavenger tests were performed to estimate the contribution of reactive species to TC degradation (Fig. S11 and Table S3). Ethylenediaminetetraacetic acid disodium salt (EDTA), bromate (BrO₃⁻), tert-butanol (TBA) and benzoquinone (BQ) were employed as the chemical traps of h⁺, e⁻, •OH and •O₂⁻, respectively. As for the photocatalytic

process, EDTA and BQ significantly hindered the TC degradation whereas the BrO_3^- and TBA were less efficient, which indicates that the h^+ and $\bullet\text{O}_2^-$ dominated the photodegradation process. For $\text{WO}_{3-x}/\text{H}_2\text{O}_2$ Fenton-like oxidation, an almost complete inhibition of TC degradation was observed with the presence of TBA whereas BQ just exhibited a minor effect. On the other hand, both EDTA and TBA resulted in a significant inhibition in photo-Fenton-like system. This indicates that the h^+ and $\bullet\text{OH}$ radicals are more produced and contributing together to TC degradation.

The oxygen vacancies (O_V) in $\text{WO}_{3-x}/\text{MoS}_2$ should be responsible for the generation of reactive species and the improvement of catalytic activity [41]. The reduced W^V centers should be in the vicinity of the $\text{W}_{\text{O}_\text{V}}$ or far away from the stoichiometric crystal that gives rise to conduction band states [31]. W^V is an optically active d^1 center, which results in a distinct blue coloration. This property makes it possible to qualitatively evaluate the O_V concentration by visual observation. Herein three WO_3 samples with different O_V concentration (Light yellow (LY) bare WO_3 , moderate O_V modified light blue (LB) WO_{3-x} , and the deep blue (DB) WO_{3-x} containing excessive O_V) were employed to

investigate the effect of O_V for activity enhancement. The hydrothermal procedure for DB WO_{3-x} preparation was same with that of LB WO_{3-x} synthesis except the dosage of $\text{C}_2\text{H}_5\text{NO}_2$ increased from 0.0113 g (0.15 mmol) to 0.0565 g (0.75 mmol). Fig. 4a shows that the W 4f XPS spectra of LB and DB WO_{3-x} samples slightly shift towards lower binding energy in comparison with that of LY WO_3 , which can be attributed to the generation of reduced W^V species. Solid EPR spectra (Fig. 4b) show that the signals of unpaired electrons in LB WO_{3-x} and DB WO_{3-x} are higher than that of LY WO_3 . This is consistent with the result of XPS analysis and indicates that a higher concentration of O_V leads to a deeper blue color of WO_{3-x} .

Time profile of TC removal shows that the moderate O_V modified LB WO_{3-x} exhibits the best activity among these catalysts (Fig. 4c). This enhanced performance can be attributed to the efficient conversion of high energy photons and the quick transfer of free electrons that leads to a fast redox process. Typically, the increased activity should be linked to the improved conductivity as a direct result of the O_V induces the increased doping density as well as enhances band bending close to the semiconductor interface where the most high energy photons are

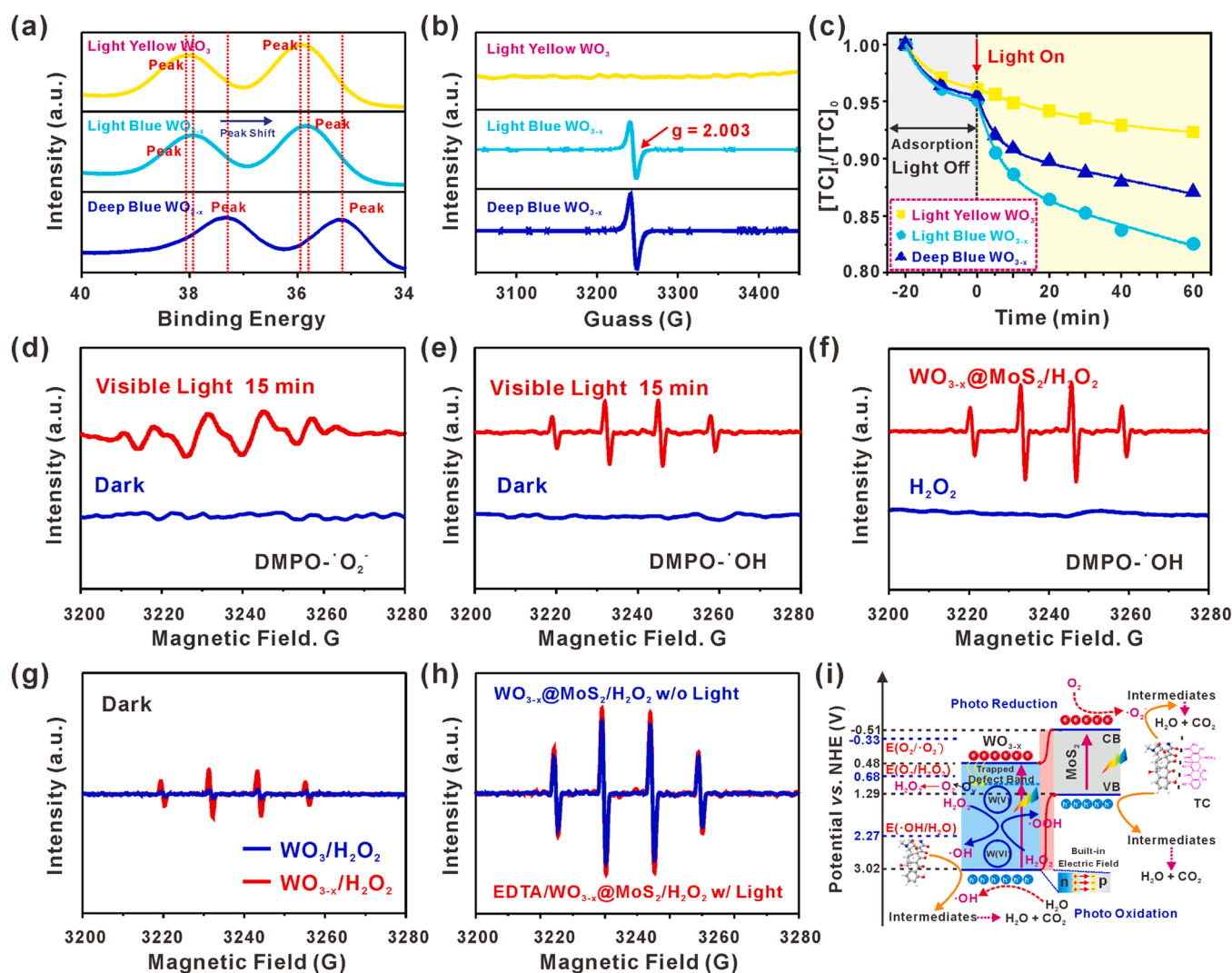


Fig. 4. (a) W 4f XPS and (b) solid EPR spectra of LY WO_{3-x} , LB WO_{3-x} and DB WO_{3-x} . (c) WO_{3-x} with different O_V concentration for photocatalytic degradation of TC. Experimental condition: [catalyst] = 0.3 g/L, $[\text{TC}]_0 = 100 \mu\text{M}$, pH = 6, visible light irradiation. Liquid EPR spectra of (d) $\text{DMPO}\cdot\text{O}_2^-$ and (e) $\text{DMPO}\cdot\text{OH}$ adducts recorded with the presence of $\text{WO}_{3-x}/\text{MoS}_2$ under visible light irradiation. (f) Liquid EPR spectra of $\text{DMPO}\cdot\text{OH}$ adducts recorded in H_2O_2 solution with and without $\text{WO}_{3-x}/\text{MoS}_2$ under the dark condition. (g) Liquid EPR spectra of $\text{DMPO}\cdot\text{OH}$ adduct recorded in $\text{WO}_3/\text{H}_2\text{O}_2$ (blue) and $\text{WO}_{3-x}/\text{H}_2\text{O}_2$ (red) systems. (h) Liquid EPR spectra of $\text{DMPO}\cdot\text{OH}$ adduct recorded in $\text{WO}_{3-x}/\text{MoS}_2/\text{H}_2\text{O}_2$ (blue) and EDTA/visible light/ $\text{WO}_{3-x}/\text{MoS}_2/\text{H}_2\text{O}_2$ (red) systems. Experimental condition: [catalyst] = 0.3 g/L, $[\text{H}_2\text{O}_2]_0 = 15 \text{ mM}$, $[\text{DMPO}]_0 \approx 100 \text{ mM}$. (i) Schematic demonstration of the energy band structure of $\text{WO}_{3-x}/\text{MoS}_2$ heterojunction and the proposed mechanism for TC degradation.

absorbed and the photogenerated carriers transfer [31]. For those samples with excessive O_V , they cannot achieve the higher activities for demanding oxidation reaction as the large amounts of oxygen defects states will severely increase the loss of driving force and thus hinder the oxidation reactions that require oxidative power, despite the increase in carriers' lifetime [31,42]. On the other hand, those samples with limited oxygen defects are unable to work for the photocatalytic reaction because of the fast charge recombination. The doping density and the concentration of the reduced elements (e.g., W_{OV} center) should be balanced to tune the activities of catalysts. Our strategy makes the charge carriers relaxation into trap states and results in a slower charge recombination while the expense of energy loss to drive catalytic reaction is not too high and thus improve the utilization of photogenerated carriers.

For liquid EPR analysis (Fig. 4d), no DMPO- $\bullet O_2$ signal was measured with WO_{3-x} @ MoS_2 under dark condition while it was observed after visible light irradiation for 15 min. The split peaks in DMPO- $\bullet O_2$ adduct can be attributed to the response of DMPOX signal that DMPO was directly oxidized by photogenerated holes [33,34]. The observed DMPO- $\bullet OH$ signal in Fig. 4e was induced via the paths of O_2 reduction ($O_2 \rightarrow H_2O_2 \rightarrow \bullet OH$) and H_2O oxidation ($H_2O \rightarrow \bullet OH + H^+$) under visible light irradiation. On the other hand, no DMPO- $\bullet OH$ signal was measured in the presence of H_2O_2 alone under dark condition while a clear signal was recorded when the catalyst was added (Fig. 4f). It

should be noted that the O_V in WO_{3-x} @ MoS_2 can induce the H_2O_2 decomposition and $\bullet OH$ incubation (e^- (trapped in O_V) + $H_2O_2 \rightarrow \bullet OH + OH^-$) under dark condition [43]. Fig. 4g shows the insignificant signal of DMPO- $\bullet OH$ adduct in WO_3/H_2O_2 dark suspension whereas it is enhanced with WO_{3-x} powders and further improved with WO_{3-x} @ MoS_2 (Fig. 4f). Additionally, EPR tests were conducted to evaluate the contribution of photo-generated electrons in photo-Fenton-like system (Fig. 4h). EDTA was employed as hole scavenger to exclude the influence from H_2O oxidation ($h^+ + H_2O \rightarrow \bullet OH + H^+$), and WO_{3-x} @ MoS_2/H_2O_2 as a control group was used to show the $\bullet OH$ production from dark Fenton-like system ($H_2O_2 \rightarrow \bullet OH + \bullet OOH$). It is clear that WO_{3-x} @ MoS_2/H_2O_2 /EDTA suspension under visible light irradiation produces more $\bullet OH$ radicals (DMPO- $\bullet OH$ adducts) via the path of H_2O_2 reduction by the photogenerated electrons ($e^-_{CB} + H_2O_2 \rightarrow \bullet OH + OH^-$). The enhanced photon utilization and carrier transfer via the p-n heterojunction structure and the introduction of defected O_V jointly facilitate the various redox processes to achieve the pollutant degradation (Fig. 4i).

Fig. 5a shows the Nyquist plots of WO_3 , WO_3 @ MoS_2 and WO_{3-x} @ MoS_2 obtained from the electrochemical impedance spectroscopy (EIS) measurements, which provides the information on the charge transfer resistance (R_{ct}). The R_{ct} value of WO_3 @ MoS_2 is smaller than that of WO_3 , and WO_{3-x} @ MoS_2 exhibits the smallest R_{ct} value among the three samples. This result is consistent with the photoactivity that

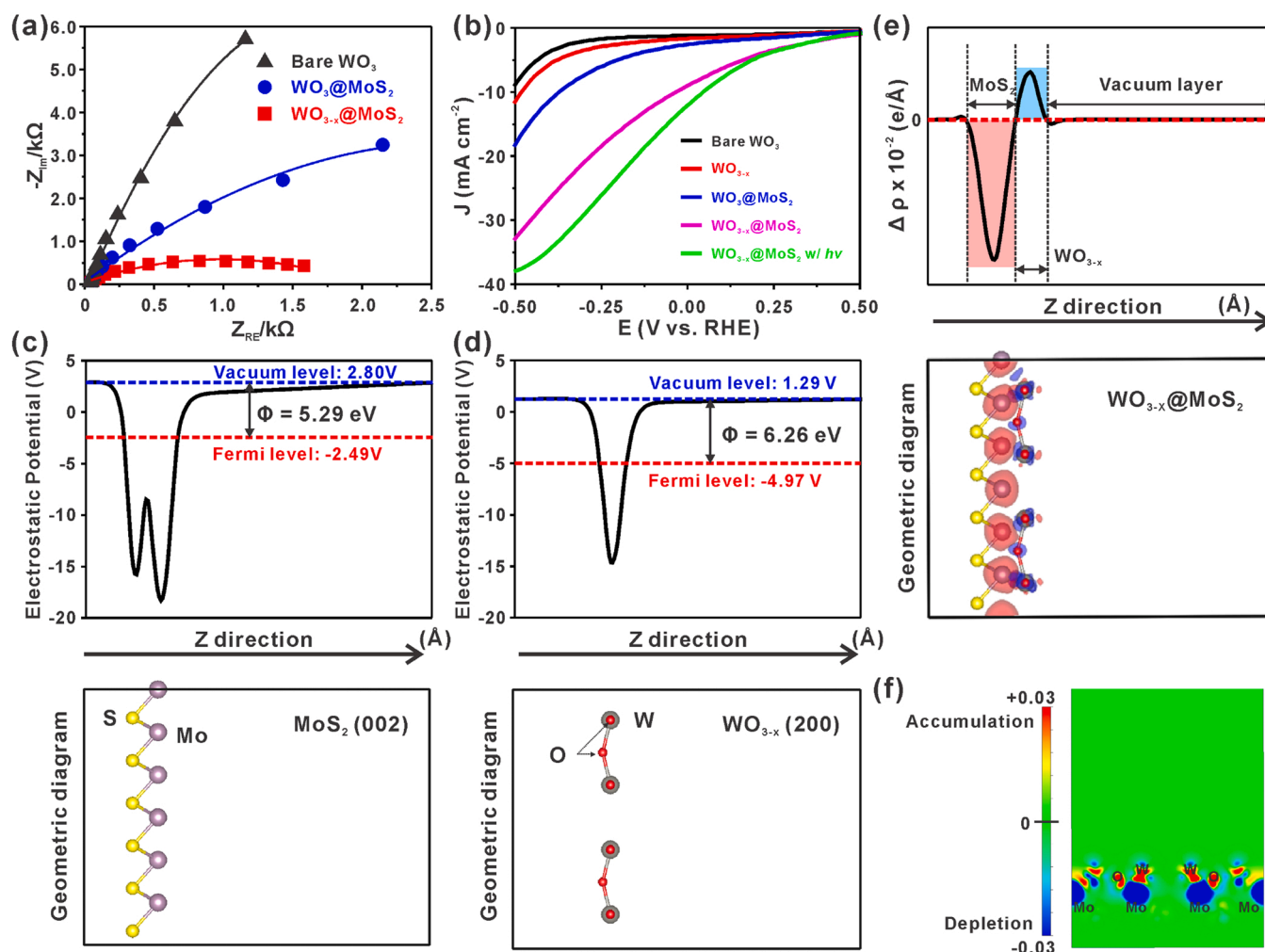


Fig. 5. (a) Nyquist plots of WO_3 , WO_3 @ MoS_2 and WO_{3-x} @ MoS_2 obtained under visible light irradiation. (b) LSV of WO_3 , WO_{3-x} , WO_3 @ MoS_2 and WO_{3-x} @ MoS_2 electrodes in Ar-saturated 0.1 M KOH solution containing 15 mM H_2O_2 . The electrostatic potentials (ESP) and the corresponding geometric structures of (c) MoS_2 and (d) WO_{3-x} . (e) Planar average charge density difference of WO_{3-x} @ MoS_2 heterojunction. (f) Electronic location function (ELF) of the interlayer, where red and blue represent charge accumulation and depletion regions, respectively.

the $\text{WO}_{3-x}@\text{MoS}_2$ exhibits the highest performance for TC degradation (Fig. 3d). Fig. 5b shows the LSV curves of bare WO_3 , WO_{3-x} , $\text{WO}_3@\text{MoS}_2$ and $\text{WO}_{3-x}@\text{MoS}_2$ measured in N_2 -saturated 0.1 M KOH solution containing 15 mM H_2O_2 . The H_2O_2 reduction current under dark condition is significantly higher with $\text{WO}_{3-x}@\text{MoS}_2$ than that with other samples and further increases under visible light irradiation.

On the other hand, the electrostatic potential (ESP) function diagrams and the corresponding geometric structures of MoS_2 and WO_{3-x} were obtained using computational calculation (Fig. 5c, d) [44]. The Fermi energy level (E_F) of WO_{3-x} is lower than that of MoS_2 , which leads to a spontaneous electrons flow from MoS_2 to WO_{3-x} until the E_F on both sides reaches the same potential. Hence the band bending occurs and the internal electric field is formed to promote the separation and transfer of the charge carriers and thus prolong their life for photoactivity enhancement. Fig. 5e shows the planar averaged charge density difference of $\text{WO}_{3-x}@\text{MoS}_2$ heterojunction along the z-direction. It is clear that the negative charge is mainly accumulated on WO_{3-x} whereas the MoS_2 is positive charged. The zero accumulation and transformation of charge carrier on both sides of the heterojunction confirms that the thickness of the vacuum layer is suitable for analytical calculations. Fig. 5f shows the electronic location function of the interlayer, with the

red and blue representing the negative charge accumulation and depletion regions, respectively. The negative charge is mainly concentrated on the surface of WO_{3-x} while the electron depletion occurred on MoS_2 . This is consistent with the result of the photoelectrochemical measurements and confirms that the electrons redistribution and band alignment favor the photo-Fenton-like reaction [45].

3.4. Intermediates identification and toxicity evaluation

LC-MS profiles of TC transformation were recorded in Fenton-like and photocatalytic processes (Fig. 6a). The detailed discussion on intermediates identification and pathway analysis was shown in Text S4, Figs. S12 and 6b. The product with $m/z = 445$ should be the parent compound TC, and its atomic numbers are marked in Fig. 6c. Fig. 6b and Table 1 show that the $\text{WO}_{3-x}@\text{MoS}_2$ hollow tube as a versatile environmental catalyst exhibits enhanced photo-Fenton-like activity in destructing TC. Herein a question remains elusive that what is the most possible pathway to proceed the dehydration process (e.g., Products 9, 10 and 11). Some literature reported that the C-H bond should be broken from the methyl group instead of carbocyclic ring, forming an ethylene linkage in the branched chain [46,47]. However, this reaction is

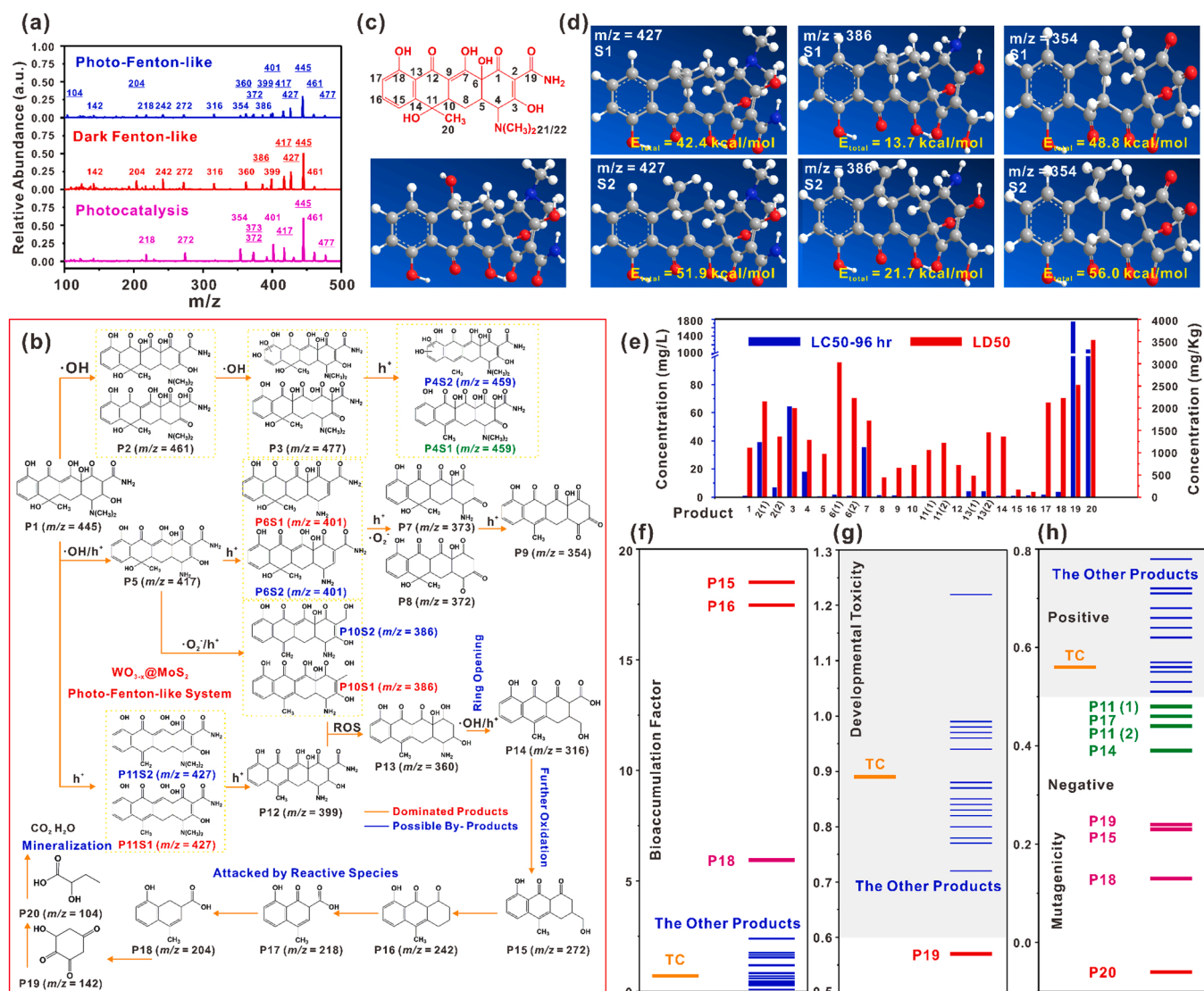


Fig. 6. (a) LC-MS spectra of TC degradation recorded in $\text{WO}_{3-x}@\text{MoS}_2$ photocatalytic process, dark Fenton-like oxidation and photo-Fenton-like system. (b) The proposed pathway of TC transformation in $\text{WO}_{3-x}@\text{MoS}_2$ photo-Fenton-like system. (c) 2D/3D molecule model of tetracycline. (d) Structural optimization of the proposed intermediates. (e) Predicted toxicity, (f) bioaccumulation factor, (g) developmental toxicity and (h) mutagenicity of TC and its intermediates.

Table 1

The proposed intermediates of TC transformation in photo-Fenton-like system.

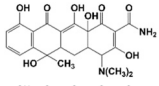
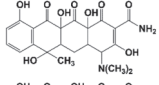
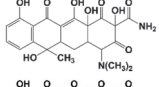
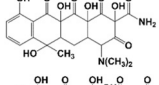
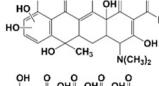
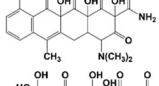
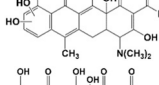
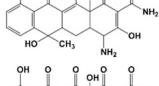
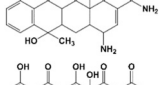
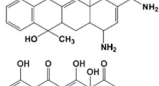
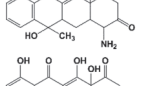
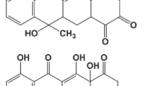
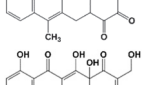
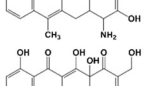
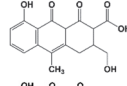
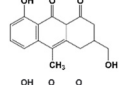
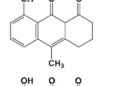
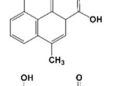
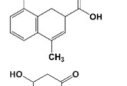
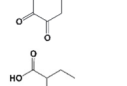
Product	This work	Ref.
Product 1 (445)		—
Product 2 (461)		[33,34,48,49]
Product 3 (477)		[33,34]
Product 4 (459)		[33,34]
Product 5 (417)		[48,49]
Product 6 (401)		[48,50]
Product 7 (373)		—
Product 8 (372)		[48]
Product 9 (354)		[33,34,46,49]
Product 10 (386)		—
Product 11 (427)		[48,51,52]
Product 12 (399)		[46,51,52]
Product 13 (360)		[46]
Product 14 (316)		—

Table 1 (continued)

Product	This work	Ref.
Product 15 (272)		[46]
Product 16 (242)		[46,48]
Product 17 (218)		[48]
Product 18 (204)		—
Product 19 (142)		—
Product 20 (104)		—

unfavorable from the view of molecular dynamics since breaking C-H bond in -CH₃ group is more difficult than that in carbocyclic ring. The computational analysis of structure design optimization confirms that the dehydrogenation process on the carbocyclic ring makes the energy of intermediates lower and is more favorable to the reaction (Fig. 6d and Table S4). Finally, these intermediates are completely ring-opened and then mineralized into CO₂, H₂O, and other inorganic residues.

The biological toxicity of TC and its intermediates was evaluated by T.E.S.T., which adopts median lethal concentration (LC50–96hr for *Daphnia*) and dosage (LD 50 for oral rat), bioaccumulation factor, developmental toxicity, and mutagenicity as the main descriptors (Table S5). Fig. 6e shows that LC50–96hr and LD50 values of P17–P20 are much higher than that of the parent compound TC, which indicates that these products turned to be “non-toxic” after the photo-Fenton-like treatment. On the other hand, the bioaccumulation factor of most intermediates was remarkably reduced in comparison with that of TC (Fig. 6f). Fig. 6g and h show that the developmental toxicity and mutagenicity of TC are classified as toxicant and positive respectively, whereas the final intermediates such as P15–P20 are considered as non-toxic and reach to a “negative” level. This indicates that the environmental risk of TC can be highly reduced using defect-engineered WO_{3-x}@MoS₂ hollow tube.

4. Conclusions

The defect-engineered WO_{3-x}@MoS₂ hollow tube exhibiting enhanced Fenton-like and photocatalytic activities via internal electric field rearrangement and band alignment has been demonstrated. It exhibits an intrinsic radical character for H₂O₂ decomposition under dark condition in a wide range of pH and an efficient photon utilization under visible light irradiation, which is clearly different from the conventional photocatalysts. The activity of WO_{3-x}@MoS₂ for tetracycline (TC) degradation can reach one to two orders of magnitude higher than that of other materials used in this work. LC-MS analysis and theoretical calculation confirm that the intermediates were turned to be “non-toxic” and their ecotoxicity decreased during the oxidation process. The present strategy of combining the Fenton-like and photocatalytic activities extends the application of the conventional photocatalysts and should be an efficient way of energy utilization.

CRediT authorship contribution statement

Yi Hu: Conceptualization, Methodology, Investigation, Visualization, Writing – original draft. **Mingxing Nie:** Formal analysis, Investigation. **Peidong Hong:** Investigation, Data curation. **Junyong He:** Formal analysis. **Yulian Li:** Investigation. **Kaisheng Zhang:** Investigation. **Dandan Yang:** Formal analysis. **Lisha Jiang:** Methodology, Formal analysis, Investigation, Resources. **Jinhui Liu:** Resources. **Lingtao Kong:** Project administration, Resources, Funding acquisition.

Declaration of Competing Interest

The authors declare that they have no known competing financial interests or personal relationships that could have appeared to influence the work reported in this paper.

Data availability

No data was used for the research described in the article.

Acknowledgments

This work was supported by the National Key Research and Development Program of China (2019YFC0408500), ("Technology boosts Economy 2020"), the Natural Science Foundation of China (21976182), the Natural Science Foundation of Anhui Province (2008085MB48, 2208085MB36) and the CASHIPS Director's Fund (No. YZJJ2021QN23). Yi Hu thanks the computational support from Supercomputing Center of University of Science and Technology of China (USTC) and Yantai University.

Appendix A. Supplementary material

Supplementary data associated with this article can be found in the online version at [doi:10.1016/j.apcatb.2022.122013](https://doi.org/10.1016/j.apcatb.2022.122013).

References

- [1] Y. Guo, S. Huang, Y. Guo, Z. Ye, J. Nan, Q. Zhou, Y. Zhu, Efficient degradation of organic pollutants by enhanced interfacial internal electric field induced via various crystallinity carbon nitride homojunction, *Appl. Catal. B Environ.* 312 (2022) 121388, <https://doi.org/10.1016/j.apcatb.2022.121388>.
- [2] K. Wang, X. Feng, Y. Shanguan, X. Wu, H. Chen, Selective CO₂ photoreduction to CH₄ mediated by dimension-matched 2D/2D Bi₃NbO₇/g-C₃N₄ S-scheme heterojunction, *Chin. J. Catal.* 43 (2022) 246–254, [https://doi.org/10.1016/s1872-2067\(21\)63819-6](https://doi.org/10.1016/s1872-2067(21)63819-6).
- [3] M.S. Koo, X. Chen, K. Cho, T. An, W. Choi, In situ photoelectrochemical chloride activation using a WO₃ electrode for oxidative treatment with simultaneous H₂ evolution under visible light, *Environ. Sci. Technol.* 53 (2019) 9926–9936, <https://doi.org/10.1038/s41467-021-22839-0>.
- [4] F. He, W. Jeon, W. Choi, Photocatalytic air purification mimicking the self-cleaning process of the atmosphere, *Nat. Commun.* 12 (2021) 2528, <https://doi.org/10.1038/s41467-021-22839-0>.
- [5] T.H. Jeon, D. Monllor-Satoca, G.H. Moon, W. Kim, H.I. Kim, D.W. Bahnemann, H. Park, W. Choi, Ag(I) ions working as a hole-transfer mediator in photoelectrocatalytic water oxidation on WO₃ film, *Nat. Commun.* 11 (2020) 967, <https://doi.org/10.1038/s41467-020-14775-2>.
- [6] S.J. Hong, S. Lee, J.S. Jang, J.S. Lee, Heterojunction BiVO₄/WO₃ electrodes for enhanced photoactivity of water oxidation, *Energy Environ. Sci.* 4 (2011) 1781–1787, <https://doi.org/10.1039/c0ee00743a>.
- [7] J. Fu, Q. Xu, J. Low, C. Jiang, J. Yu, Ultrathin 2D/2D WO₃/g-C₃N₄ step-scheme H₂-production photocatalyst, *Appl. Catal. B Environ.* 243 (2019) 556–565, <https://doi.org/10.1016/j.apcatb.2018.11.011>.
- [8] T. Cai, Y. Liu, L. Wang, S. Zhang, J. Ma, W. Dong, Y. Zeng, J. Yuan, C. Liu, S. Luo, "Dark deposition" of Ag nanoparticles on TiO₂: improvement of electron storage capacity to boost "memory catalysis" activity, *ACS Appl. Mater. Interfaces* 10 (2018) 25350–25359, <https://doi.org/10.1021/acsami.8b06076>.
- [9] Y.-D. Chiou, Y.-J. Hsu, Room-temperature synthesis of single-crystalline Se nanorods with remarkable photocatalytic properties, *Appl. Catal. B Environ.* 105 (2011) 211–219, <https://doi.org/10.1016/j.apcatb.2011.04.019>.
- [10] Y. Yin, L. Shi, W. Li, X. Li, H. Wu, Z. Ao, W. Tian, S. Liu, S. Wang, H. Sun, Boosting Fenton-like reactions via single atom Fe catalysis, *Environ. Sci. Technol.* 53 (2019) 11391–11400, <https://doi.org/10.1021/acs.est.9b03342>.
- [11] X. Li, X. Huang, S. Xi, S. Miao, J. Ding, W. Cai, S. Liu, X. Yang, H. Yang, J. Gao, J. Wang, Y. Huang, T. Zhang, B. Liu, Single cobalt atoms anchored on porous N-doped graphene with dual reaction sites for efficient Fenton-like catalysis, *J. Am. Chem. Soc.* 140 (2018) 12469–12475, <https://doi.org/10.1021/jacs.8b05992>.
- [12] C. Zhao, S. Guo, Q. Li, J. Liu, M. Zheng, X. Xiao, B. Jiang, H. Fu, Supramolecular precursor derived loofah sponge-like Fe₂O₃/C for effective synergistic reaction of Fenton and photocatalysis, *Nano Res.* 15 (2021) 1949–1958, <https://doi.org/10.1007/s12274-021-3838-5>.
- [13] H. Zhang, S. Wang, Y. Wang, J. Yang, X. Gao, L. Wang, TiO₂(B) nanoparticle-functionalized WO₃ nanorods with enhanced gas sensing properties, *Phys. Chem. Chem. Phys.* 16 (2014) 10830–10836, <https://doi.org/10.1039/c4cp00356j>.
- [14] K. Ghosh, A. Roy, S. Tripathi, S. Ghule, A.K. Singh, N. Ravishanker, Insights into nucleation, growth and phase selection of WO₃: morphology control and electrochromic properties, *J. Mater. Chem. C* 5 (2017) 7307–7316, <https://doi.org/10.1039/c7tc01714f>.
- [15] Y. Hu, P. Zhang, J. Du, C. Kim, S. Han, W. Choi, Bifunctional carbon nitride exhibiting both enhanced photoactivity and residual catalytic activity in the post-irradiation dark period, *ACS Catal.* 11 (2021) 14941–14955, <https://doi.org/10.1021/acscatal.1c04564>.
- [16] H. Sun, F. He, W. Choi, Production of reactive oxygen species by the reaction of periodate and hydroxylamine for rapid removal of organic pollutants and waterborne bacteria, *Environ. Sci. Technol.* 54 (2020) 6427–6437, <https://doi.org/10.1021/acs.est.0c00817>.
- [17] L. Jiang, J. Li, K. Wang, G. Zhang, Y. Li, X. Wu, Low boiling point solvent mediated strategy to synthesize functionalized monolayer carbon nitride for superior photocatalytic hydrogen evolution, *Appl. Catal. B Environ.* 260 (2020) 118181, <https://doi.org/10.1016/j.apcatb.2019.118181>.
- [18] K. Wang, H. Wang, Q. Cheng, C. Gao, G. Wang, X. Wu, Molecular-functionalized engineering of porous carbon nitride nanosheets for wide-spectrum responsive solar fuel generation, *J. Colloid Interface Sci.* 607 (2022) 1061–1070, <https://doi.org/10.1016/j.jcis.2021.09.034>.
- [19] W. Fan, B. Zhang, X. Wang, W. Ma, D. Li, Z. Wang, M. Dupuis, J. Shi, S. Liao, C. Li, Efficient hydrogen peroxide synthesis by metal-free polyterthiophene via photoelectrocatalytic dioxygen reduction, *Energy Environ. Sci.* 13 (2020) 238–245, <https://doi.org/10.1039/c9ee02247c>.
- [20] Y. Wang, B. Zhu, B. Cheng, W. Macyk, P. Kuang, J. Yu, Hollow carbon sphere-supported Pt/CoO hybrid with excellent hydrogen evolution activity and stability in acidic environment, *Appl. Catal. B Environ.* 314 (2022) 121503, <https://doi.org/10.1016/j.apcatb.2022.121503>.
- [21] P. Hong, Z. Wu, D. Yang, K. Zhang, J. He, Y. Li, C. Xie, W. Yang, Y. Yang, L. Kong, J. Liu, Efficient generation of singlet oxygen (¹O₂) by hollow amorphous Co/C composites for selective degradation of oxytetracycline via Fenton-like process, *Chem. Eng. J.* 421 (2021), 129594, <https://doi.org/10.1016/j.cej.2021.129594>.
- [22] Z. Wang, L. Jiang, K. Wang, Y. Li, G. Zhang, Novel AgI/Bi₂SO₄ heterojunction for efficient photocatalytic degradation of organic pollutants under visible light: interfacial electron transfer pathway, DFT calculation and degradation mechanism study, *J. Hazard. Mater.* 410 (2021), 124948, <https://doi.org/10.1016/j.jhazmat.2020.124948>.
- [23] K. Wang, L. Jiang, T. Xin, Y. Li, X. Wu, G. Zhang, Single-atom V-N charge-transfer bridge on ultrathin carbon nitride for efficient photocatalytic H₂ production and formaldehyde oxidation under visible light, *Chem. Eng. J.* 429 (2022), <https://doi.org/10.1016/j.cej.2021.132229>.
- [24] X. Chen, Z. Wang, X. Wang, R. Zhang, X. Liu, W. Lin, Y. Qian, Synthesis of novel copper sulfide hollow spheres generated from copper (II)-thiourea complex, *J. Cryst. Growth* 263 (2004) 570–574, <https://doi.org/10.1016/j.jcrysgro.2003.12.004>.
- [25] G. Lin, J. Zheng, R. Xu, Template-free synthesis of uniform CdS hollow nanospheres and their photocatalytic activities, *J. Phys. Chem. C* 112 (2008) 7363–7370, <https://doi.org/10.1021/jp800696v>.
- [26] Y. Guo, X. Wang, W. Shao, Facile one-step synthesis of SnS₂ nanoscale hollow spheres for enhanced lithium-ion storage performance as anode, *Micro Nano Lett.* 13 (2018) 1269–1271, <https://doi.org/10.1049/mnl.2018.5125>.
- [27] N. Zheng, G. Jiang, X. Chen, J. Mao, N. Jiang, Y. Li, Battery separators functionalized with edge-rich MoS₂/C hollow microspheres for the uniform deposition of Li₂S in high-performance lithium-sulfur batteries, *Nano-Micro Lett.* 11 (2019) 43, <https://doi.org/10.1007/s40820-019-0275-z>.
- [28] Y. Zeng, N. Guo, H. Li, Q. Wang, X. Xu, Y. Yu, X. Han, H. Yu, A novel route to manufacture WO₃@MoS₂ p-n heterostructure hollow tubes with enhanced photocatalytic activity, *Chem. Commun.* 55 (2019) 683–686, <https://doi.org/10.1039/c8cc08614a>.
- [29] C. Chen, H. Zeng, M. Yi, G. Xiao, S. Xu, S. Shen, B. Feng, In-situ growth of Ag₃PO₄ on calcined Zn-Al layered double hydroxides for enhanced photocatalytic degradation of tetracycline under simulated solar light irradiation and toxicity assessment, *Appl. Catal. B Environ.* 252 (2019) 47–54, <https://doi.org/10.1016/j.apcatb.2019.03.083>.
- [30] Z. Sun, R. Huo, C. Choi, S. Hong, T.-S. Wu, J. Qiu, C. Yan, Z. Han, Y. Liu, Y.-L. Soo, Y. Jung, Oxygen vacancy enables electrochemical N₂ fixation over WO₃ with tailored structure, *Nano Energy* 62 (2019) 869–875, <https://doi.org/10.1016/j.nanoen.2019.06.019>.
- [31] M. Sachs, J.S. Park, E. Pastor, A. Kafizas, A.A. Wilson, L. Francas, S. Gul, M. Ling, C. Blackman, J. Yano, A. Walsh, J.R. Durrant, Effect of oxygen deficiency on the excited state kinetics of WO₃ and implications for photocatalysis, *Chem. Sci.* 10 (2019) 5667–5677, <https://doi.org/10.1039/c9sc00693a>.
- [32] W. Wei, Y. Yao, Q. Zhao, Z. Xu, Q. Wang, Z. Zhang, Y. Gao, Oxygen defect-induced localized surface plasmon resonance at the WO_{3-x} quantum dot/silver nanowire

- interface: SERS and photocatalysis, *Nanoscale* 11 (2019) 5535–5547, <https://doi.org/10.1039/c9nr01059a>.
- [33] L. Ren, W. Zhou, B. Sun, H. Li, P. Qiao, Y. Xu, J. Wu, K. Lin, H. Fu, Defects-engineering of magnetic γ -Fe₂O₃ ultrathin nanosheets/mesoporous black TiO₂ hollow sphere heterojunctions for efficient charge separation and the solar-driven photocatalytic mechanism of tetracycline degradation, *Appl. Catal. B Environ.* 240 (2019) 319–328, <https://doi.org/10.1016/j.apcatb.2018.08.033>.
- [34] Z. Xie, Y. Feng, F. Wang, D. Chen, Q. Zhang, Y. Zeng, W. Lv, G. Liu, Construction of carbon dots modified MoO₃/g-C₃N₄ Z-scheme photocatalyst with enhanced visible-light photocatalytic activity for the degradation of tetracycline, *Appl. Catal. B Environ.* 229 (2018) 96–104, <https://doi.org/10.1016/j.apcatb.2018.02.011>.
- [35] J. Meng, Q. Lin, T. Chen, X. Wei, J. Li, Z. Zhang, Oxygen vacancy regulation on tungsten oxides with specific exposed facets for enhanced visible-light-driven photocatalytic oxidation, *Nanoscale* 10 (2018) 2908–2915, <https://doi.org/10.1039/c7nr08590g>.
- [36] X. Xing, H. Zhu, M. Zhang, L. Hou, Q. Li, J. Yang, Interfacial oxygen vacancy layer of a Z-scheme BCN–TiO₂ heterostructure accelerating charge carrier transfer for visible light photocatalytic H₂ evolution, *Catal. Sci. Technol.* 8 (2018) 3629–3637, <https://doi.org/10.1039/c8cy01035h>.
- [37] B. Song, T. Wang, H. Sun, Q. Shao, J. Zhao, K. Song, L. Hao, L. Wang, Z. Guo, Two-step hydrothermally synthesized carbon nanodots/WO₃ photocatalysts with enhanced photocatalytic performance, *Dalton Trans.* 46 (2017) 15769–15777, <https://doi.org/10.1039/c7dt03003g>.
- [38] X. Gao, K. Gao, F. Fu, C. Liang, Q. Li, J. Liu, L. Gao, Y. Zhu, Synergistic introducing of oxygen vacancies and hybrid of organic semiconductor: realizing deep structure modulation on Bi₅O₇I for high-efficiency photocatalytic pollutant oxidation, *Appl. Catal. B Environ.* 265 (2020), 118562, <https://doi.org/10.1016/j.apcatb.2019.118562>.
- [39] S.S. Kalanur, Y.J. Hwang, S.Y. Chae, O.S. Joo, Facile growth of aligned WO₃ nanorods on FTO substrate for enhanced photoanodic water oxidation activity, *J. Mater. Chem. A* 1 (2013) 3479–3488, <https://doi.org/10.1039/c3ta01175e>.
- [40] S.A. Ansari, M.M. Khan, S. Kalathil, A. Nisar, J. Lee, M.H. Cho, Oxygen vacancy induced band gap narrowing of ZnO nanostructures by an electrochemically active biofilm, *Nanoscale* 5 (2013) 9238–9246, <https://doi.org/10.1039/c3nr02678g>.
- [41] G. Zhuang, Y. Chen, Z. Zhuang, Y. Yu, J. Yu, Oxygen vacancies in metal oxides: recent progress towards advanced catalyst design, *Sci. China Mater.* 63 (2020) 2089–2118, <https://doi.org/10.1007/s40843-020-1305-6>.
- [42] R. Lin, J. Wan, Y. Xiong, K. Wu, W.C. Cheong, G. Zhou, D. Wang, Q. Peng, C. Chen, Y. Li, Quantitative study of charge carrier dynamics in well-defined WO₃ nanowires and nanosheets: insight into the crystal facet effect in photocatalysis, *J. Am. Chem. Soc.* 140 (2018) 9078–9082, <https://doi.org/10.1021/jacs.8b05293>.
- [43] H. Li, J. Shang, Z. Yang, W. Shen, Z. Ai, L. Zhang, Oxygen vacancy associated surface Fenton chemistry: surface structure dependent hydroxyl radicals generation and substrate dependent reactivity, *Environ. Sci. Technol.* 51 (2017) 5685–5694, <https://doi.org/10.1021/acs.est.7b00040>.
- [44] K. Wang, X. Shao, K. Zhang, J. Wang, X. Wu, H. Wang, 0D/3D Bi₃TaO₇/ZnIn₂S₄ heterojunction photocatalyst towards degradation of antibiotics coupled with simultaneous H₂ evolution: in situ irradiated XPS investigation and S-scheme mechanism insight, *Appl. Surf. Sci.* 596 (2022), <https://doi.org/10.1016/j.apsusc.2022.153444>.
- [45] K. Wang, Q. Wang, K. Zhang, G. Wang, H. Wang, Selective solar-driven CO₂ reduction mediated by 2D/2D Bi₂O₂SiO₃/MXene nanosheets heterojunction, *J. Mater. Sci. Technol.* 124 (2022) 202–208, <https://doi.org/10.1016/j.jmst.2021.10.059>.
- [46] J. Cao, Z.-h Yang, W.-p Xiong, Y.-y Zhou, Y.-r Peng, X. Li, C.-y Zhou, R. Xu, Y.-r Zhang, One-step synthesis of Co-doped UiO-66 nanoparticle with enhanced removal efficiency of tetracycline: simultaneous adsorption and photocatalysis, *Chem. Eng. J.* 353 (2018) 126–137, <https://doi.org/10.1016/j.cej.2018.07.060>.
- [47] L. Chen, X. Zuo, S. Yang, T. Cai, D. Ding, Rational design and synthesis of hollow Co₃O₄@Fe₂O₃ core-shell nanostructure for the catalytic degradation of norfloxacin by coupling with peroxydisulfate, *Chem. Eng. J.* 359 (2019) 373–384, <https://doi.org/10.1016/j.cej.2018.11.120>.
- [48] S. Kumar Ray, D. Dhakal, G. Gyawali, B. Joshi, A. Raj Koirala, S. Wahn Lee, Transformation of tetracycline in water during degradation by visible light driven Ag nanoparticles decorated α -NiMoO₄ nanorods: mechanism and pathways, *Chem. Eng. J.* 373 (2019) 259–274, <https://doi.org/10.1016/j.cej.2019.05.041>.
- [49] Q. Zhu, Y. Sun, F. Na, J. Wei, S. Xu, Y. Li, F. Guo, Fabrication of CdS/titanium-oxo-cluster nanocomposites based on a Ti₃₂ framework with enhanced photocatalytic activity for tetracycline hydrochloride degradation under visible light, *Appl. Catal. B Environ.* 254 (2019) 541–550, <https://doi.org/10.1016/j.apcatb.2019.05.006>.
- [50] M.-R. Li, G.-C. Wang, Differentiation of the C–O and C–C bond scission mechanisms of 1-hexadecanol on Pt(111) and Ru(0001): a first principles analysis, *Catal. Sci. Technol.* 7 (2017) 743–760, <https://doi.org/10.1039/c6cy02529c>.
- [51] N. Alberro, M. Torrent-Sucarrat, A. Arrieta, G. Rubiales, F.P. Cossio, Density functional theory study on the demethylation reaction between methylamine, dimethylamine, trimethylamine, and tamoxifen catalyzed by a Fe(IV)-Oxo porphyrin complex, *J. Phys. Chem. A* 122 (2018) 1658–1671, <https://doi.org/10.1021/acs.jpca.7b10654>.
- [52] L. Zhao, N. Nakatani, Y. Sunada, H. Nagashima, J.Y. Hasegawa, Theoretical study on the rhodium-catalyzed hydrosilylation of C=C and C=O double bonds with tertiary silane, *J. Org. Chem.* 84 (2019) 8552–8561, <https://doi.org/10.1021/acs.joc.9b00959>.